POLITECNICO DI TORINO
Repository ISTITUZIONALE

A Compact Sub-THz Horn-Based Imaging System with Potential Application to Non-invasive Contactless Skin Cancer Detection

Original
A Compact Sub-THz Horn-Based Imaging System with Potential Application to Non-invasive Contactless Skin Cancer Detection / Moda, S., Paonessa, F., Tobon Vasquez, J.A., Virone, G., Vipiana, F.. - In: IEEE TRANSACTIONS ON ANTENNAS AND PROPAGATION. - ISSN 1558-2221. - (In corso di stampa).

Availability:
This version is available at: 11583/3015168 since: 2026-09-04T10:42:44Z

Publisher:
IEEE

Published
DOI:

Terms of use:

This article is made available under terms and conditions as specified in the corresponding bibliographic description in the repository

Publisher copyright
IEEE postprint/Author's Accepted Manuscript

©9999 IEEE. Personal use of this material is permitted. Permission from IEEE must be obtained for all other uses, in any current or future media, including reprinting/republishing this material for advertising or promotional purposes, creating new collecting works, for resale or lists, or reuse of any copyrighted component of this work in other works.

(Article begins on next page)

20 November 2026

A Compact Sub-THz Horn-Based Imaging System with Potential Application to Non-invasive Contactless Skin Cancer Detection

Stefano Moda, *Student member, IEEE*, Fabio Paonessa *Member, IEEE*, Jorge A. Tobón Vasquez *Member, IEEE*, Giuseppe Virone *Senior Member, IEEE* and Francesca Vipiana, *Senior Member, IEEE*

***Abstract*—Terahertz waves have attracted increasing interest in the research community for skin cancer diagnosis owing to their sensitivity to water molecules, typically more abundant in tumors than in healthy tissues, and their non-invasive nature. In this work, a compact, contactless continuous-wave system employing a diagonal horn antenna is introduced and experimentally assessed in the $500-750$ GHz band. The system capabilities are experimentally quantified using dedicated phantoms that reproduce the dielectric contrast between basal cell carcinoma and healthy skin. To this end, a methodology for dielectric characterization in the $500-750$ GHz band and the fabrication of solid, easily reproducible phantoms is presented, integrating experimental and numerical data via dedicated look-up tables. The obtained experimental results, supported by detectability and measurement uncertainty analyses, indicate promising capabilities of the proposed compact contactless system for sub-THz skin imaging applications.**

***Index Terms*—Biomedical applications of radiation, Dielectric Measurement, Phantoms, Terahertz wave imaging.**

I. Introduction

SKIN cancer, in its widest definition, is regarded as the most common form of cancer, encompassing melanoma and non-melanoma types. According to the American Cancer Society, more than 100,000 cases of melanoma and approximately 5.4 million cases of Basal Cell Carcinoma (BCC) and Squamous Cell Carcinoma (SCC) were diagnosed in the United States in 2025 [1]. Given current epidemiological trends, early diagnosis and effective treatment are essential to address the growing global incidence and the associated health and socioeconomic burden [2], [3].

Biomedical imaging and sensing devices constitute a *sine qua non* in modern clinical practice. Although skin cancer diagnosis primarily relies on visual inspection, non-invasive optical imaging techniques, including Reflectance Confocal Microscopy (RCM), Optical Coherence Tomography (OCT) and dermoscopy, are employed. However, these modalities primarily provide morphological or structural information and may suffer from limited penetration depth due to optical scattering and absorption in tissue. As a result, lesion characterization largely relies on the visual interpretation of morphological features and clinician expertise. Consequently, histological examination of biopsy samples remains the gold standard for definitive diagnosis, despite its invasive nature.

Terahertz (THz) and sub-THz waves, on the other hand, provide functional contrast by probing tissue water content, making them increasingly attractive for biomedical imaging [4], [5]. Their high sensitivity to tissue water content arises from their interaction with collective motions in the hydrogen bond network of water molecules [6]. Since malignant tissue generally exhibits higher water content than healthy tissue, this difference constitutes an intrinsic contrast mechanism for lesion detection. Their wavelengths ranging from tens of micrometers to millimeters, also enable higher spatial resolution than microwave-based approaches, while their low photon energy makes them intrinsically non-ionizing.

The first experimental studies on the interaction of THz waves with healthy and diseased skin were reported about two decades ago in [15], [16], where reflection-geometry Time Domain Spectroscopy (TDS) enabled the first *ex vivo* and *in vivo* imaging of BCC lesions by exploiting the intrinsic contrast associated with tissue water content. TDS illuminates the material under test (MUT) with trains of picosecond pulses containing a broad frequency distribution centered around 1 THz, providing coherent amplitude and phase measurements over a wide bandwidth and yielding spectral information across multiple frequencies simultaneously [17]. However, for the application addressed in this work, the dielectric contrast between BCC and healthy skin has been reported to reach its maximum in the $500-700$ GHz range (Fig. 1) [18], [19]. In TDS systems, multiple time domain acquisitions are typically averaged to improve the signal-to-noise ratio (SNR), with the acquisition time depending on the selected averaging settings. TDS systems have traditionally relied on free-space optical configurations, while recent fiber-coupled architectures have enabled more compact handheld probes, including systems employed for *in-vivo* skin investigations [12]. However, these implementations generally remain contact-based, with reference windows, often made of quartz, placed directly against the skin. More recently, even smaller TDS probes have also

This work has been supported in part by the PNRR-NGEU project, funded by the Ministry of University and Research (MUR, DM118/2023), by the research project "MedWaveImage", funded by Interreg Central Europe (CE0200670), and by the research project "3BAtwin" funded by the Horizon EU FP (101159623).

Stefano Moda and Francesca Vipiana are with the Department of Electronics and Telecommunications, Politecnico di Torino, 10129 Torino, Italy (e-mail: stefano.moda@polito.it; francesca.vipiana@polito.it).

Jorge Alberto Tobón Vásquez is with Wavision S.r.l., 10129 Torino, Italy (e-mail: jorge.tobon@wavision.it).

Fabio Paonessa and Giuseppe Virone are with the Institute of Electronics, Information and Telecommunications Engineering, Consiglio Nazionale delle Ricerche, 10129 Torino, Italy (e-mail: fabio.paonessa@cnr.it; giuseppe.virone@cnr.it).

TABLE I
COMPARISON WITH RELATED WORKS ON SKIN SENSING AND IMAGING

Ref.	Frequency range	System type	Contactless	Sensor type
[7]	$12-110\,\mathrm{GHz}$	CW, VNA	Yes	four Vivaldi antennas
[8]	$15-110\,\mathrm{GHz}$	CW, VNA	No	dielectric-filled open waveguide
[9]	$94-104\,\mathrm{GHz}$	CW, VNA	No	near-field probe
[10]	$140-210\,\mathrm{GHz}$	CW, VNA	No	horn antenna with quasi-optical system
[11]	$90-300\,\mathrm{GHz}$	CW, VNA	No	glass-filled open waveguide
[12]	$0.1-1\,\mathrm{THz}$	THz-TDS	No	handheld optical system
[13]	$1.39\,\mathrm{THz}$, $1.63\,\mathrm{THz}$	CW, laser	Yes	optical system
[14]	$2.85\,\mathrm{THz}$	CW, laser	No	optical system
[15], [16]	$0.1-3\,\mathrm{THz}$	THz-TDS	No	optical system
This work	$500-750\,\mathrm{GHz}$	CW, VNA	Yes	diagonal horn antenna

emerged [20], although their application to clinical skin investigations remains unexplored. When the probe is pressed against the skin, hydration accumulates in the upper cutaneous layers due to porous obstruction, altering the natural water content and affecting the measurements [21].

Unlike TDS techniques, continuous-wave (CW) systems employ single-tone signals swept over a defined frequency range, enabling a high SNR. The acquisition time is determined by the selected sweep parameters, intermediate-frequency (IF) bandwidth, and averaging settings and can therefore be tailored to the specific application. CW systems also readily operate in a monostatic configuration, providing the potential for the RF hardware to be integrated into compact measurement probes. Nevertheless, many implementations remain contact-based, bulky, or rely on high-power sources (e.g., laser-based systems), limiting their applicability in practical scenarios. Table I summarizes representative works on THz and sub-THz techniques for skin sensing and imaging, illustrating the diversity of approaches in the current landscape.

In this study, we present a compact CW horn-based system with a $250\,\mathrm{GHz}$ bandwidth covering the $500-750\,\mathrm{GHz}$ range. To assess its potential in skin cancer detection, we develop a dedicated, easily fabricated and reproducible phantom mimicking a BCC embedded into a healthy skin background, and we propose a methodology for solid material characterization at these frequencies, aiming to replicate dielectric contrasts consistent with those reported in the literature for biological tissues. To the best of the authors' knowledge, this is the first system combining a compact-probe contactless VNA-based setup with reflection-mode operation above $110\,\mathrm{GHz}$ for skin cancer applications (see Table I). Differently from pulsed TDS systems, which typically rely on bulky optical setups, and from CW laser-based systems, which require high-power sources unsuitable for clinical use, the proposed system is based on a vector network analyzer (VNA) architecture and emits less than $70\,\mu\mathrm{W}$ at the small probe aperture (3 mm), enabling a compact and intrinsically safe configuration.

The present article is organized as follows. Section II presents the phantom design and fabrication methodology for the $500-750\,\mathrm{GHz}$ band, including the characterization procedure of the constituent materials and the verification of consistency with the natural contrast measured on real skin samples. Section III describes the designed measurement system, detailing its components, operational principles, and the acquisition parameters. Section IV reports the experimental results obtained from the proposed phantoms, highlighting the contactless system's potential to detect BCC regions in skin tissue. Finally, in Sect. V the work conclusion and perspectives are reported.

Preliminary numerical investigations have been performed in the recent conference paper [22].

II. PHANTOM FABRICATION AND CHARACTERIZATION

The use of phantoms that mimic the physical properties of biological tissues is, for ethical and practical reasons, essential during the experimental phases of developing new biomedical detection techniques. A tissue-mimicking phantom, that is easy to fabricate and reliably reproducible, plays a key role in the validation and design of any new system. In the context of microwave and millimeter-wave–based technologies, phantoms must reasonably emulate the dielectric properties of tissues, such as relative permittivity (ε_r) and electrical conductivity (σ). Pathology-driven changes in these properties yield distinct electromagnetic signatures, enabling detection of the underlying condition.

A. Healthy Skin and BCC Dielectric Contrast

Relatively few studies report measurements on human samples in the sub-THz range, and even fewer focus on tumor tissues [23]. At such high frequencies, the strong dependence of dielectric properties on water content means that factors such as temperature, anatomical site, subject age, and whether the sample is measured *in-vivo* or *ex-vivo* contribute significantly to the variability and uncertainty of reported data. Skin structure itself varies across anatomical locations within the same individual, and its hydration level likewise differs, typically decreasing with age. Since measurements performed on in-vitro cultured skin samples under controlled conditions minimize extrinsic variability, allowing the observed dielectric differences to be more confidently attributed to the pathology itself, we rely on the permittivity and conductivity values of healthy and BCC-affected skin reported by Nourinovin *et al.* [18], [19], obtained through transmission TDS. As shown in Appendix A, these measurements reveal differences between

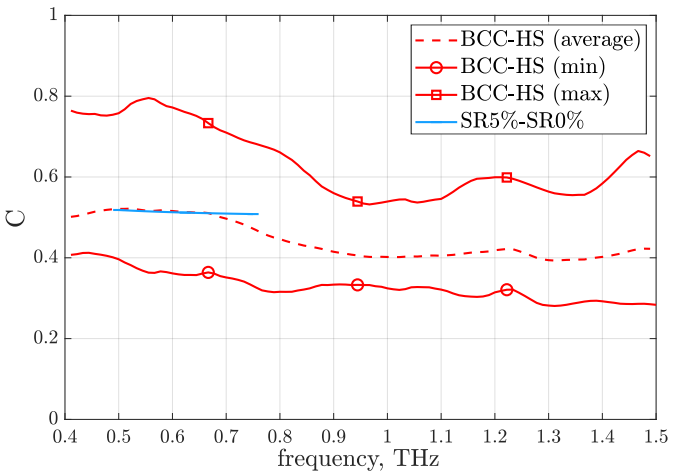


Fig. 1. Dielectric contrast between basal cell carcinoma (BCC) and healthy skin (HS), indicated in red, and between 5% and 0% graphite-loaded silicone rubber (SR), indicated in cyan.

the two conditions, whose frequency-dependent dielectric contrast can be quantified as

$$C(f) = \left| \frac{\tilde{\varepsilon}_{bg} - \tilde{\varepsilon}_{tg}}{\tilde{\varepsilon}_{bg}} \right|, \tag{1}$$

where $\tilde{\varepsilon}_{bg}$ and $\tilde{\varepsilon}_{tg}$ denote the complex permittivity of the background (i.e., healthy skin) and the target (i.e., basal cell carcinoma), respectively. Figure 1 shows the dielectric contrast between the BCC target and the healthy-skin (HS) background, computed from the values in [18], [19] (also reported in Appendix A). The contrast reaches its maximum around 550 GHz. The average contrast (dash-dotted line in Fig. 1) shows a maximum region in the 500–750 GHz band. This result stimulated the selection of such a frequency band in the present research activity.

B. Phantom and Samples Fabrication

Phantoms can be produced in liquid, solid, and semi-solid formats. Liquid phantoms are easy to prepare but are prone to degradation due to evaporation, resulting in a limited lifetime. Mirbeik-Sabzevari *et al.* in [24] proposed a semi-solid skin-mimicking phantom composed of water, oil, and gelatin, characterized up to 50 GHz only. By adjusting the relative proportions of its ingredients, this phantom can also emulate BCC-affected skin. However, this type of phantom requires a complex preparation process and specific precautions to ensure long-term stability.

Among solid phantoms, those made from silicone- or urethane-based rubber materials stand out for their ease of preparation and long lifetime, and are widely used for microwave applications [25]. Christ *et al.* in [26] employed a graphite-loaded silicone rubber phantom produced by SPEAG and characterized it up to 110 GHz.

In this work, we develop an easily reproducible skin model, extending the dielectric characterization of silicone–graphite mixtures up to the WR-1.5 band (500 − 750 GHz), corresponding to the frequency range where the contrast between BCC and healthy skin (HS) is maximum (see Sect. II-A).

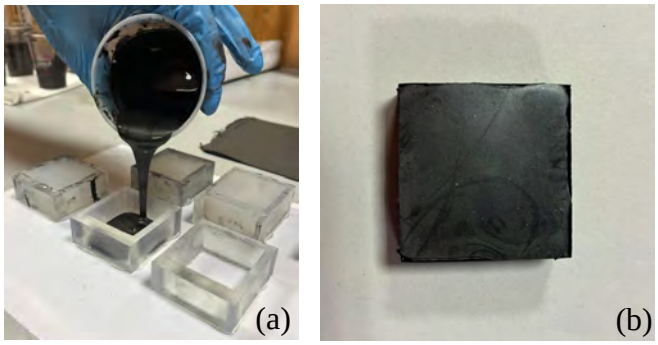


Fig. 2. The making of the silicone samples. (a): pouring of the silicone rubber and graphite mixture into the molds; (b): dried sample extracted from the mold (b).

To this end, a set of resin molds are 3D-printed to provide the desired geometry to the silicone mixtures during the curing phase. The silicone material comes as a bicomponent liquid formulation that polymerizes into a solid elastomer once mixed. The amount of graphite added to the mixture prior to curing allows tuning of the resulting dielectric properties. For dielectric characterization, one pure-silicone sample and two additional samples, containing 5% and 10% graphite percent weight respectively, are prepared. To improve mixing efficiency and ensure sample homogeneity, the graphite powder is first blended with one of the two silicone components before the two parts are mixed together. Particular care must be taken at this step to ensure a homogeneous compound, which is then poured into the molds once properly blended, as shown in Fig. 2(a). The viscosity of the mixture can hinder the release of entrapped air bubbles; therefore, the use of a vacuum chamber improves the efficiency of degassing. After the two silicone components are combined, the samples cure in approximately four hours and, thanks to the intrinsic stability of the material, are not susceptible to degradation over time. An example of a final sample is shown in Fig. 2(b).

C. Phantom Dielectric Characterization

To characterize the dielectric properties of the fabricated silicone samples in the 500 − 750 GHz band, we assemble a measurement setup consisting of a WR-1.5 waveguide section (see Fig. 3) connected to a VDI WM-380 VNAX extension module [27], which is in turn connected to a Rohde & Schwarz ZNA67 VNA [28]. In this configuration, the extension module is mounted vertically and held in place by a support stand. A one-port offset-short, short, matched-load (OSM) calibration is performed at the waveguide output flange. The graphite-silicone samples are positioned on a height-adjustable laboratory jack and raised into contact with the waveguide, enabling acquisition of the reflection coefficients (S_{11}) [Fig. 3(a)].

Since an open-ended waveguide pressed against a soft and elastic material (i.e. the graphite-silicone sample) may cause the sample to protrude into the aperture and affect the measurement [29], we record the reflection coefficient (S_{11}) while varying the applied force. This is achieved by placing an electronic scale between the elevation jack and the sample

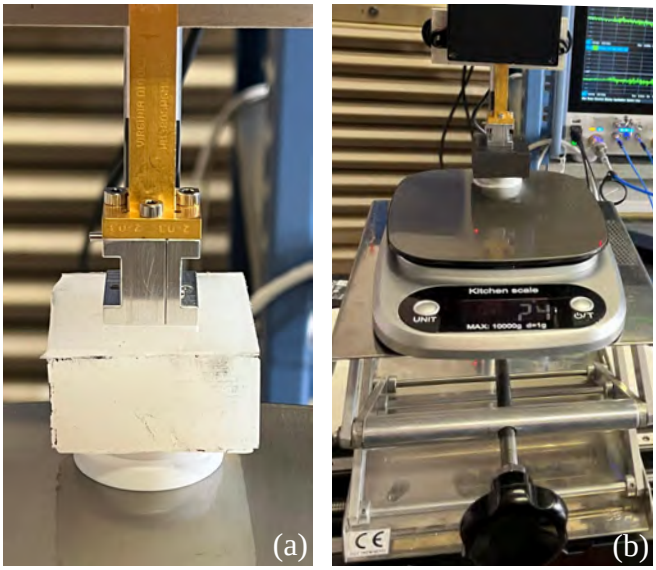


Fig. 3. Dielectric characterization of the silicone rubber samples. (a): close-up of an open-ended WR-1.5 waveguide in contact with the MUT; (b): measurement electronic scale on the elevation jack used to monitor the sample contact force.

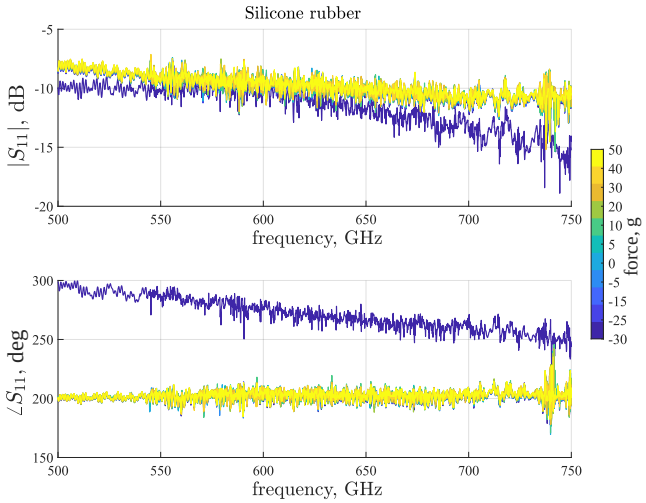


Fig. 4. Reflection coefficients of a pure silicone rubber sample at varying contact pressures with the open-ended waveguide; negative force values indicate persistent contact caused by the sample's adhesive behavior while lowering the laboratory jack, with detachment at -30 g.

to monitor the load between each acquisition, as shown in Fig. 3(b). The electronic scale is zeroed with the weight of the sample under test, so that a reading of 0 g corresponds to a no-pressure contact between the sample surface and the waveguide aperture. Figure 4 reports the magnitude and phase of the measured S_{11} for a pure silicone-rubber sample under different applied pressures; we can observe that no significant variations are present within the applied range of pressure. This behavior is likely attributable to the mechanical properties of the sample combined with the small dimensions of the waveguide aperture ($380 \times 190\,\mu m$). It should be pointed out that the negative force values are achieved due to slight short-term adhesive properties of the silicone rubber (i.e., the scale is pulling the sample). After removing the visible outlier (blue curve in Fig. 4) acquired right after sample–probe separation, the remaining measurements are averaged to denoise the data, leaving only calibration-related residuals. Such results are shown in Fig. 5 (black lines).

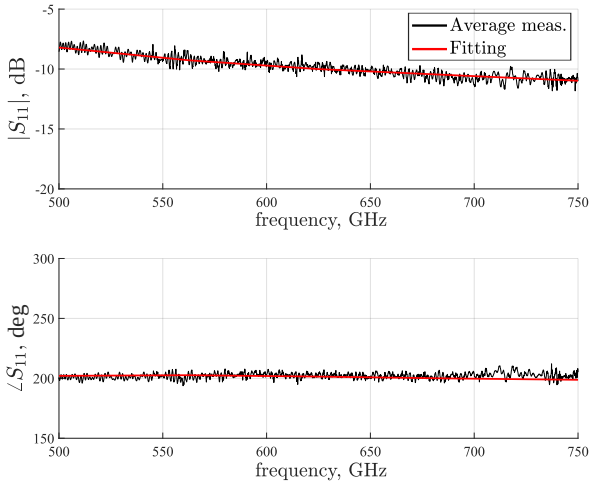


Fig. 5. Reflection coefficients averaged over applied pressure, measured with an open-ended waveguide in contact with a pure silicone rubber sample (black lines) and obtained from fitted full-wave simulations (red lines).

A numerical model of the probe–sample interaction is developed in CST Studio Suite [see Fig. 6(a)] to accurately represent the open-ended waveguide in contact with the MUT. After confirming through preliminary simulations that the probe flange does not perturb the field distribution, the model size is minimized using symmetry planes and reflection-free boundaries, thereby reducing computational cost without compromising accuracy.

Such a model is then employed to perform parametric full-wave simulations with parametric variations of the MUT permittivity and conductivity. The resulting data are used to construct look-up tables that capture the transfer function of the system, showing how changes in dielectric properties translate into corresponding variations of the measured S_{11}. Figure 7 presents the look-up table computed at 625 GHz. The response is sufficiently monotonic with nearly orthogonal iso-ε_r and

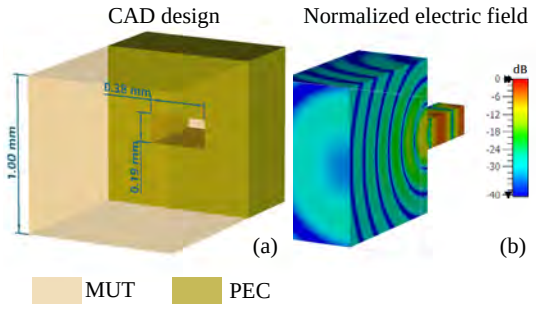


Fig. 6. Numerical model used for parametric full-wave simulations. (a): CAD design; (b): normalized electric field distribution.

iso-σ contours, ensuring a unique correspondence between the

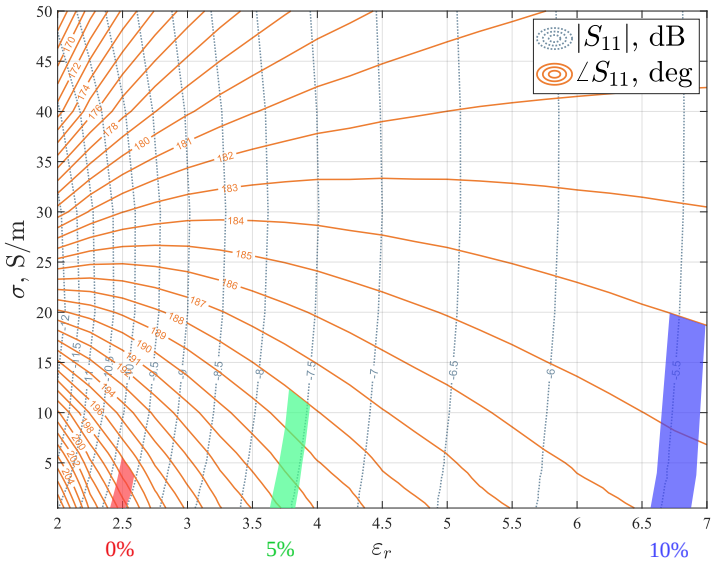


Fig. 7. Look-up table at 625 GHz showing the transfer function of the open-ended waveguide for MUT characterization: the orange and blue curves represent the magnitudes and phases of the reflection coefficients, respectively. The regions highlighted in red, green and blue have been determined as an envelope of the measured S_{11} values of the silicone rubber samples with 0%, 5%, and 10% graphite percent weight, respectively.

measured coefficients and the underlying dielectric parameters. Figure 7 also shows three colored regions corresponding to the measured S_{11} values of the silicone rubber samples with 0%, 5%, and 10% graphite weight, respectively. The extension of the regions is determined considering repeatability of the measurements, which is mainly due to residual calibration errors and slight non-uniformity of the samples.

For the case of a pure silicone rubber sample (i.e., 0% of graphite), the numerical response computed by assigning the extracted dielectric properties to the full-wave model is also reported in Fig. 5 with red lines. The agreement with measured data is remarkable within the full frequency band. In the fitting we assume constant dielectric properties across the frequency range given the water-free and homogeneous nature of our phantoms. Similar level of agreement is obtained also for the other samples.

The contrast determined from measured 5% graphite-loaded silicone (SR5%) and the pure silicone (SR0%) samples in the WR-1.5 band is also reported in Fig. 1 with the cyan curve. It falls within the range defined by the maximum and minimum BCC–HS contrasts reported in the literature and closely matches the average value. Accordingly, the adopted phantom materials are consistent with the average dielectric contrast between BCC and HS. A more realistic representation of the layered, heterogeneous, dispersive, and hydration-dependent behaviour of biological skin will be considered in future work.

Based on these results, a set of skin phantoms is fabricated using SR0% as the background and SR5% as the target, to replicate the scenario of a BCC lesion embedded within healthy skin. These structures can be easily cast into different geometries, with the target shape and size determined by the prepared molds. The set of skin phantoms is fabricated with both smooth and rough surfaces and with increasing target size to assess the system imaging and detectability performance. Figure 8(a) depicts an example of such skin phantoms featuring a rough surface and a target with nominal dimension of 1 mm, while Fig. 8(b) shows the corresponding surface images of a smooth-surface skin phantom set acquired using a Mitutoyo Quick Vision Active measurement system. Similar data were obtained for the rough samples.

III. Horn-based contactless measurement system

As mentioned in the introduction, a compact antenna is used to perform contactless reflectivity measurements of the skin phantom samples. Such a probe is a WR-1.5-fed diagonal horn, featuring a nominal gain of 26 dBi and a full half-power beamwidth (FHPBW) of approximately 10°. The size of the waveguide flange, shown in Fig. 9, is 19 mm, whereas the horn itself fits within an envelope of $9 \times 9 \times 27$ mm^3. The aperture size is 3 mm only, therefore, further miniaturization is still possible to achieve even more compact and portable solutions.

As shown in Fig. 9, the horn is mounted to the extender flange, corresponding to the calibration plane, and oriented downward to achieve a monostatic configuration. The sample under test is positioned below the horn at a distance of about 13 mm, so in a contactless configuration. It should be noted that such a value is smaller than the Fraunhofer distance (38 mm at 625 GHz), therefore, the sample lies in the near-field of the horn. This condition has been set up to achieve a more focused field distribution on the sample, leading to better lateral resolution with respect to the far-field condition.

A tilt stage is used to hold the sample and set the angle-of-incidence of the impinging wave. It is mounted on a laboratory jack, which is in turn installed on a motorized linear translation stage, providing a repeatability of 6 μm and a maximum travel range of 300 mm [30]. The combined use of the tilt stage and the elevation jack enables the exploration of different configurations in terms of angle-of-incidence and stand-off distance. During each acquisition session, the linear stage executes a scan of 20 mm with a step size of 300 μm. For each sample position, the VNA performs a frequency sweep over the full module operating band 500 − 750 GHz. Software-based triggering is implemented to ensure consistency between position and reflection measurements.

Each acquired S_{11} trace consists of 1001 uniformly-spaced frequency points. The adopted frequency step corresponds to a maximum unambiguous range of about 600 mm, which, combined with the inherently high propagation losses in the 500 − 750 GHz range, ensures effective suppression of undesired multipath contributions and multiple-reflection artifacts in the measured response.

The VNA is configured with a 1 kHz IF bandwidth to achieve a proper trade-off between dynamic range and sweep time. A dwell time of 0.7 s is inserted between the end of each frequency sweep and the subsequent stage movement to allow data transfer at each scan position. The combination of the scanning mechanism and VNA settings provides an overall scan time of about five minutes.

A standard OSM calibration is performed directly at the extender flange prior to each measurement session, establish-

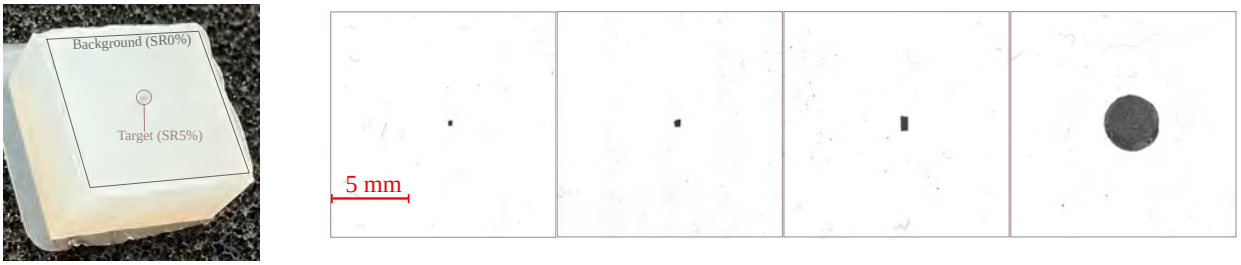


Fig. 8. Silicone-based skin phantoms. (a): Rough-surface phantom mimicking a basal cell carcinoma of 1 mm size, surrounded by healthy skin; (b): set of smooth-surface phantoms mimicking basal cell carcinoma with increasing target size and varying shapes, embedded in a healthy skin background.

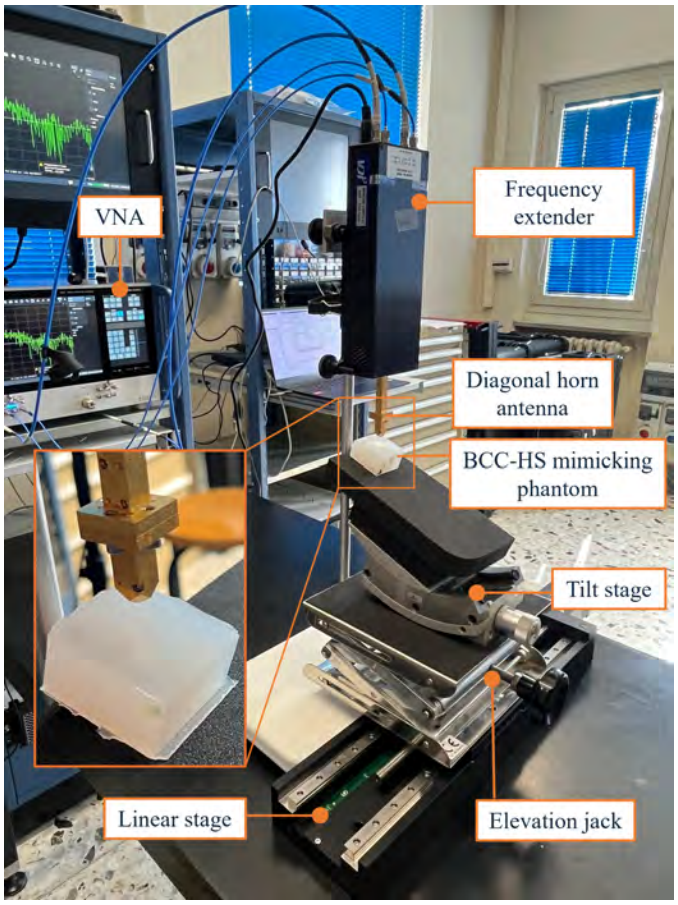


Fig. 9. Measurement setup for skin phantoms mimicking basal cell carcinoma comprising a VNA, the compact probe held vertically by a metal stand, the tilt stage, the elevation jack, and the high-precision linear stage. Close-up: the horn antenna scanning a phantom.

ing the reference plane at the waveguide aperture. The horn antenna and the subsequent free-space propagation path are therefore included in the measurement, and the acquired reflection coefficients represent the overall system response. The data are then processed in the spatial domain, as discussed in Sect. IV, to extract reflectivity profiles, enabling the separation of contributions associated with different propagation paths and the identification of the air–phantom interface response.

IV. Experimental Results and Discussion

The reflection coefficients from the skin phantoms, fabricated as described in Sect. II-B, are measured in the whole frequency band ($500-750$ GHz) using the system proposed in Sect. III. From the pointwise measured reflection coefficients, the axial reflectivity profiles, $R[n]$, are obtained to investigate the capability of identifying the presence of a BCC lesion surrounded by healthy skin. The data are transformed from the frequency domain to the spatial domain, yielding the backscattered response as a function of propagation depth. To this end, a cos^3-shaped tapering window is applied to the complex reflection coefficients prior to the inverse fast Fourier transform (IFFT) to reduce truncation effects and improve the representation of the scattered contributions:

$$R[n] = \mathrm{IFFT}\left\{w[k]S_{11}[k]\right\}, \tag{2}$$

where k and n denote the discrete frequency and spatial indices, respectively, and $w[k]$ is the adopted tapering window. The combination of the total available bandwidth and the selected window yielded an equivalent axial resolution of approximately 1.2 mm.

The axial reflectivity profiles exhibit distinct features associated with the propagation path, as shown in Fig. 10, where the profiles for all scan positions across a phantom surface are displayed. The origin of the depth axis corresponds to the calibration plane, indicated with (A) in Fig. 10. Instead, the peak labeled as (B) in Fig. 10 refers to the horn aperture. As expected, the region between (A) and (B) shows a consistent morphology across all acquisitions because it refers to inner part of the horn. The peaks corresponding to the air-phantom interface are labeled as (C) in Fig. 10. Their varying amplitudes arise from the variation of the dielectric contrast during the linear scan near the target. The distance between peaks (B) and (C) in the axial reflectivity profiles is consistent with the actual separation between the horn aperture and the phantom surface (stand-off distance). Finally, the peaks appearing beyond 50 mm in depth are attributed to reflections between the bottom surface of the phantom and the metallic surface of the elevation jack. Although very low in amplitude, their presence indicates that the wave propagates through the entire thickness of the phantom, which is a homogeneous medium. Multiple reflections from the horn aperture, its flange and the phantom interface also occur after 50 mm.

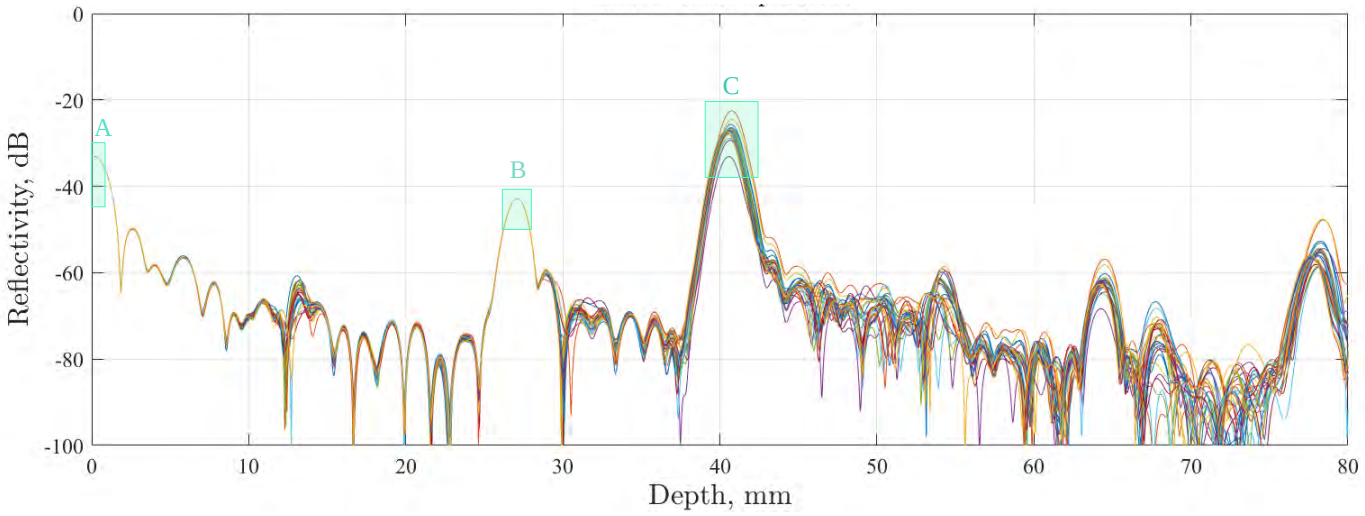


Fig. 10. Axial reflectivity profiles highlighting the calibration plane (A), antenna–air interface (B), and air–phantom interface (C), with each color corresponding to a distinct point along the scanning trajectory.

A. *Configuration Study*

The contactless system is evaluated under different geometric configurations to assess the effects of both the incidence angle of the impinging wave and the antenna–phantom stand-off distance. For both investigations, the same phantom is employed, featuring a target with a characteristic size of 1 mm and a smooth surface. By means of the tilt stage in Fig. 9, the phantom can be oriented from normal incidence to higher incidence angles while maintaining a constant stand-off distance.

The reflectivity values at the air–phantom interface [see zone (C) in Fig. 10] can be represented as a function of the lateral scan position, yielding a lateral reflectivity profile. In this representation, the target response is centered at 0 mm. For example, Fig. 11 shows lateral reflectivity profiles over a 12 mm scan for increasing angles of incidence up to 25°. The scattering background at −72 dB becomes visible from 25°. Therefore this value has been considered as the maximum incidence angle for this work.

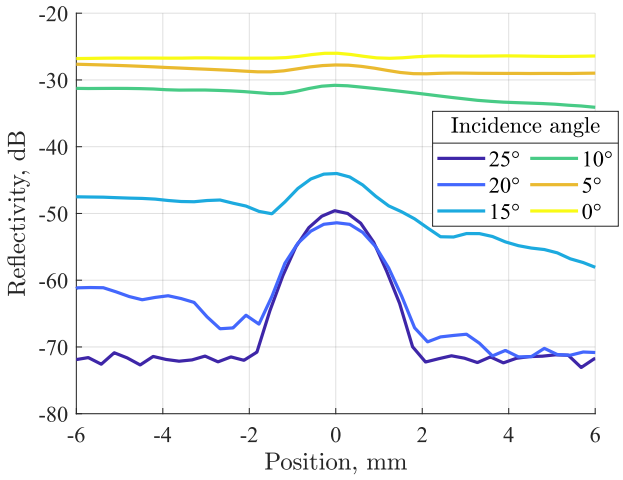


Fig. 11. Lateral reflectivity profiles at the air–phantom interface as a function of lateral position over a 12 mm scan across the target, centered at 0 mm, for different angles of incidence.

To quantitatively assess detectability, a signal-to-background ratio (SBR) is introduced, defined as the ratio between the average magnitude of the lateral reflectivity within the region of interest centered on the target peak and the average background level evaluated over symmetric regions along the scanning trajectory. With reference to Fig. 11, a higher SBR is observed at larger incidence angles, reaching 13.6 dB and 21.7 dB for 20° and 25°, respectively, despite an overall reduction in the signal level. This behavior is attributed to the locally smooth surface of the phantom, which produces predominantly specular reflections. As the incidence angle increases, the specular component is progressively redirected away from the antenna, reducing the background level, while the target, due to its dielectric discontinuity, continues to contribute to the backscattered signal. This also explains the slopes occasionally observed in the background regions which are related to the planarity error of the phantoms. Under normal incidence, the SBR is approximately 0.6 dB, indicating limited contrast between target and background. A background subtraction technique can enhance detectability in this configuration; however, this is not investigated in this work, since an incidence angle of 20° already provides high performance, especially for smaller targets.

Motivated by the higher contrast observed around 20°, measurements are performed at different antenna-sample distances, while keeping the incidence angle fixed at 20°. The lateral resolution is estimated from the 3 dB width of the scattering peak, i.e., the full width at half maximum (FWHM) of the target response under near-field conditions. The obtained values range from approximately 1.5 mm at a stand-off distance of 7 mm to about 4 mm above 30 mm. Within

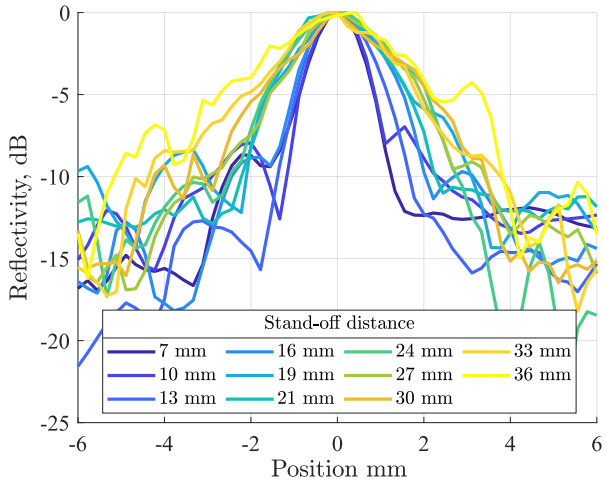


Fig. 12. Normalized lateral reflectivity profiles at the air–phantom interface for a 1 mm target, as a function of lateral position for different stand-off distances between the horn aperture and the phantom surface.

the investigated range, no abrupt degradation is observed, although the spatial extent of the response associated with the target of 1 mm size increases progressively with distance, as shown in Fig. 12. At the same time, shorter stand-off distances lead to increased sensitivity to positioning errors. Therefore, a distance of 13 mm is selected as a trade-off between lateral resolution and positioning repeatability.

B. Detectability Analysis

Phantoms with targets of increasing size are investigated under different measurement configurations, as well as smooth and rough surface conditions. These phantoms are scanned at a fixed stand-off distance of 13 mm under both normal and 20° incidence. The corresponding lateral reflectivity profiles are shown in Fig. 13, while in Fig. 14 the signal-to-background ratio versus the target size is reported.

The measured profiles confirm the analysis presented in Sect. IV-A, showing that oblique scanning enhances detectability by reducing the specular background contribution. Under these conditions, a smooth-surface phantom with a target diameter of 0.5 mm yields an SBR of 16.4 dB, indicating a very well-defined contrast against the background, whereas for the smallest scanned target (0.3 mm in size) the SBR decreases to about 3 dB, indicating reduced separation from the background level [see the green and yellow solid lines, respectively, in Fig. 13(a), and the red solid line in Fig. 14]. For the 3 mm target, the lateral reflectivity profile exhibits two distinct peaks associated with the target boundaries, rather than a single central maximum. This leads to a lower SBR, despite a broader spatial response, highlighting a limitation of peak-based SBR metrics for targets larger than 3 mm size. This effect can be attributed to the finite beam footprint, which becomes smaller than the target size, resulting in a dominant contribution from edge scattering.

For phantoms with rough surfaces, the increased scattering introduces additional background fluctuations. Under oblique incidence, the SBR is about 10.5 dB for the 0.5 mm target and 4.7 dB for the 0.3 mm target [see the green and yellow solid lines, respectively, in Fig. 13(b), and the blue solid line in Fig. 14].

For the considered dielectric contrast, consistent with that reported in the literature between BCC and HS, these results indicate that the detectability threshold is approached for target sizes around 0.3 mm, while 0.5 mm targets remain clearly detectable.

C. Uncertainty Budget

Measurement uncertainty analysis is performed to quantify the impact of different error sources on the system performance. In particular, three main contributions are considered: calibration uncertainty, system drift, and position repeatability. Each contribution is evaluated separately in order to isolate its effect and avoid cross-dependencies between different error

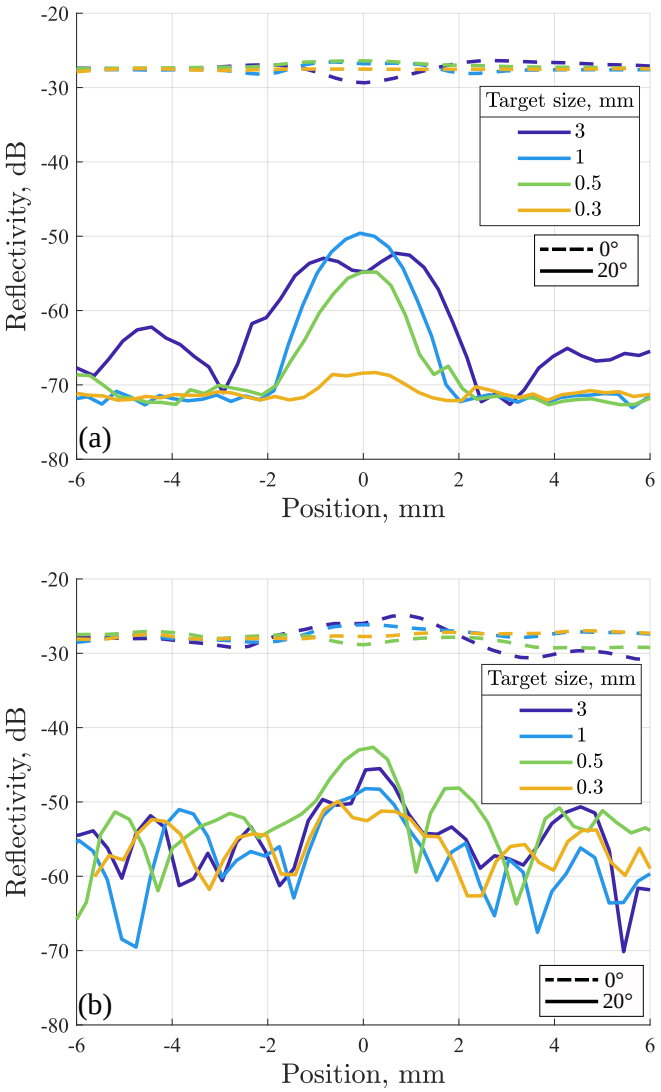


Fig. 13. Lateral reflectivity profiles at the air–phantom interface as a function of lateral position over a 12 mm scan across the target, centered at 0 mm, for phantoms with decreasing target size and different surface conditions: (a) smooth surface and (b) rough surface.

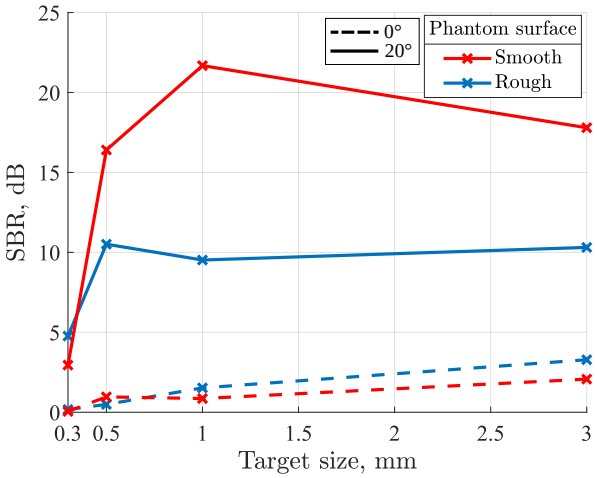


Fig. 14. Signal-to-background ratio versus target size for smooth and rough surface phantoms under normal (0°) and oblique (20°) incidence.

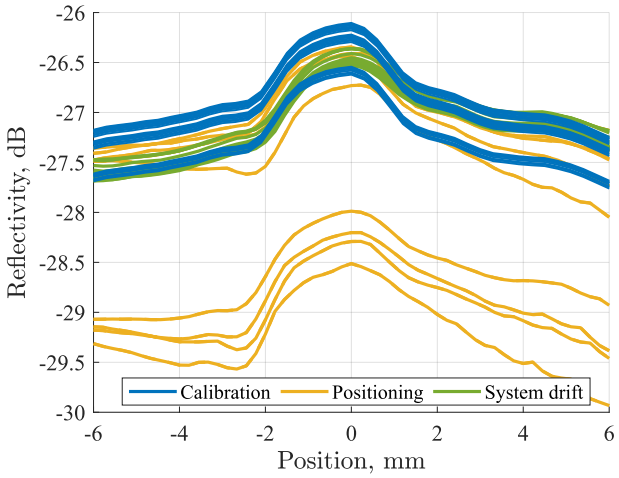


Fig. 15. Lateral reflectivity profiles at the air–phantom interface as a function of lateral position over a 12 mm scan across the target, with measurements grouped according to the investigated uncertainty contributions: calibration (blue), positioning (yellow), and system drift (green).

sources. All tests are performed using the same configuration and sample, consisting of a smooth-surface phantom with a target of nominal size 0.5 mm, scanned at a fixed stand-off distance of 13 mm and an incidence angle of 20°. The corresponding measurements are reported in Fig. 15, where the results are grouped according to the three considered contributions.

Since the system is designed to detect relative contrast between target and background, the impact of each uncertainty source is quantified in terms of the variability of the SBR. For each test, repeated measurements are carried out by varying the relevant parameter (position, time, or calibration), and the standard deviation of the resulting SBR values is used as a metric of uncertainty.

To estimate the calibration uncertainty on the reflection coefficient S_{11}, an analytical model of the one-port VNA calibration error is employed, leading to the de-embedding equation [31]:

$$S_{11} = \frac{S_{11m} - e_{11}}{e_{22}S_{11m} - \Delta}, \tag{3}$$

where S_{11m} is the raw (uncalibrated) reflection coefficient measured by the VNA, e_{11} is the directivity error, e_{22} the source match, and Δ the reflection tracking. These error terms are determined from measurements of the calibration standards. A set of 27 independent calibrations is obtained by combining three repeated measurements for each of the three calibration standards. Each calibration is then applied offline to the same raw scan of the phantom, and the resulting lateral reflectivity profiles are processed to compute the SBR. As shown in Fig. 15 (see blue lines), the resulting SBR values cluster into three distinct groups, indicating a high level of repeatability. This clustering is consistent with the three repeated measurements of the offset short standard, which appears to be the dominant source of variability among the calibration standards. In particular, the offset short introduces a phase delay along the waveguide and, with its high reflection, it is more sensitive to alignment tolerances. The SBR values obtained across all calibration combinations exhibit a standard deviation of $2.8 \cdot 10^{-4}$ dB, indicating a negligible overall impact of calibration uncertainty.

Then, the system drift is evaluated through 20 scans of the same phantom acquired at a fixed position at 30-minute intervals (see green lines in Fig. 15). The standard deviation of the SBR over the 10-hour measurement period is $6.4 \cdot 10^{-3}$ dB, indicating good stability over the considered time interval.

Finally, positioning uncertainty is evaluated through 10 scans acquired under identical geometric conditions and calibration, with the phantom repositioned around the same location under the antenna. In this case, we can recognize a vertical shift in the measured lateral reflectivity of the order of a few dB (see yellow lines in Fig. 15), although without significantly modifying neither the profile shape nor the SBR, providing a SBR standard deviation of $3.5 \cdot 10^{-2}$ dB.

Table II summarizes the standard deviations of the SBR associated with the considered uncertainty sources, along with the maximum relative error, defined as the maximum absolute deviation from the mean SBR, expressed in dB. Among the considered contributions, positioning uncertainty represents the dominant source of variability, exceeding the other terms by at least one order of magnitude. However, its absolute value remains limited, indicating that the overall measurement uncertainty is low and that the system can provide stable and repeatable measurements in prospective clinical scenarios.

TABLE II
SIGNAL-TO-BACKGROUND RATIO UNCERTAINTY BUDGET

Contribution	Standard deviation, dB	Error max, dB
Positioning uncertainty	$3.5 \cdot 10^{-2}$	$7.2 \cdot 10^{-2}$
System drift	$6.4 \cdot 10^{-3}$	$1.5 \cdot 10^{-2}$
Calibration uncertainty	$2.8 \cdot 10^{-4}$	$5.2 \cdot 10^{-4}$

D. B-scan Images

By arranging the depth-resolved axial reflectivity profiles in sequence along the linear scanning direction and mapping their amplitude to a colormap, the data can be visualized as a B-scan image. This representation is shown in Fig. 16, where each column corresponds to a single A-scan (i.e., one axial reflectivity profile), while the color encodes the signal intensity, producing a two-dimensional image in which spatial position and propagation depth are jointly displayed. In these images, acquired from phantoms with a target size of $0.5\,\mathrm{mm}$ under 20° incidence, the targets are clearly distinguishable at the correct spatial locations. This confirms the capability of the CW system to accurately differentiate a potential BCC from the surrounding healthy skin in the WR-1.5 band. For smooth-surface samples [Fig. 16(a)], the response is dominated by the target contribution, which appears clearly localized along the scanning direction. In contrast, phantoms with rough surfaces [Fig. 16(b)] exhibit localized intensity variations due to diffuse scattering from surface irregularities. Nevertheless, the target response remains clearly visible in both cases.

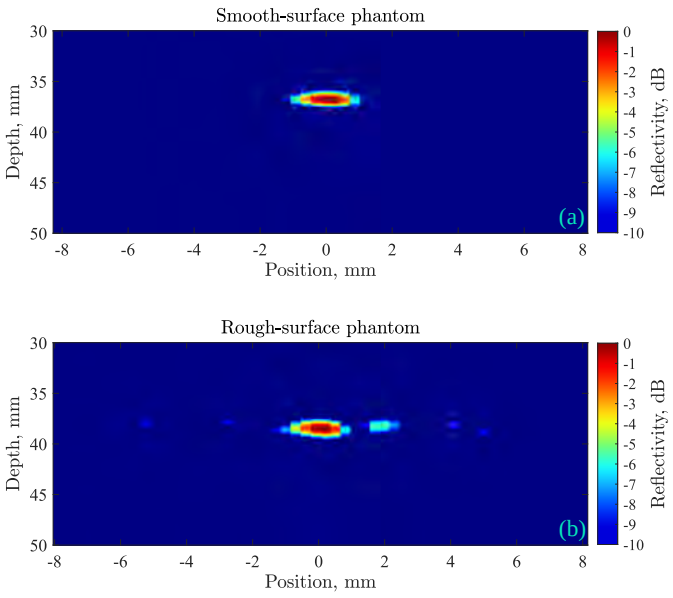


Fig. 16. B-scan images, obtained as a sequence of consecutive axial reflectivity profiles, of silicone rubber phantoms featuring a central target mimicking a skin lesion of $0.5\,\mathrm{mm}$ in size, surrounded by healthy skin, acquired with the contactless system at 20° incidence. (a): smooth-surface phantom; (b): rough-surface phantom.

V. Conclusion and Perspectives

This work presented a compact contactless CW system for generating bio-images and detecting cancer-related localized dielectric variations.

The marked dielectric contrast between BCC and healthy skin observed in the $500 - 750\,\mathrm{GHz}$ range was exploited to develop dedicated skin phantoms. An open-ended waveguide, combined with full-wave numerical simulations, was employed to characterize solid materials in this frequency band and guide the fabrication of phantoms reproducing the average dielectric contrast between BCC and healthy skin. Based on this methodology, a series of graphite-loaded silicone-rubber phantoms with different target sizes and surface conditions was fabricated and used to assess the capabilities of the proposed CW system under different measurement configurations, including varying incidence angle and stand-off distance. The SBR was adopted as a quantitative metric to evaluate target detectability and measurement repeatability throughout the study. The horn antenna ensured fully contactless operation, while the overall system successfully generated B-scan images that clearly detected the synthetic lesions embedded in the phantom. The obtained results further support the potential of sub-THz CW systems for detecting localized dielectric targets, demonstrating the feasibility of CW imaging in the upper sub-THz band.

When considering clinical applications, additional factors may influence the measured contrast, including variability in tissue hydration, the multilayer structure of the skin, and subject motion during acquisition. Variations in hydration may affect the absolute dielectric properties of both target and surrounding tissue; however, the proposed approach relies on relative contrast, which may mitigate the impact of uniform shifts in dielectric properties. The presence of multiple skin layers may introduce additional reflections and modify the overall response; nevertheless, since such contributions vary smoothly over the scanned region, they are expected to act as a common factor and have a limited impact on the relative contrast. Real skin lesions may not be perfectly planar and may exhibit local protrusions or curvature. Under such conditions, part of the scattered field is redirected away from the antenna due to local variations in surface orientation. This phenomenon may alter the measured response since surface morphology can influence the backscattered signal in addition to dielectric contrast. A possible mitigation strategy, to be investigated in future work, consists of combining scattered signals acquired under different angles of incidence. Finally, motion effects can be minimized by decreasing the acquisition time through appropriate selection of measurement parameters, enabling faster scanning procedures compatible with clinical use.

The next step of the work is the experimental validation of the proposed system on *ex-vivo* and subsequently *in-vivo* human skin malignancies under clinically representative conditions.

Appendix A
Skin Dielectric Properties

At THz frequencies, the dielectric response of skin is influenced by water content and tissue composition. However, measured dielectric properties may significantly vary depending on the adopted measurement technique, sample preparation, and biological conditions. Skin dielectric properties vary not only among individuals, but also across anatomical regions of the same subject. In addition, the skin hydration level is affected by several physiological factors, including age and perspiration activity, which may also be influenced by

mental stress conditions [32]. Overall, many factors contribute to the variability of the measured dielectric response, while only a limited number of THz dielectric characterizations of skin, especially for pathological conditions such as BCC, are currently available in the literature. For this reason, in the present work, the dielectric properties reported by Nourinovin *et al.* [18], [19] for healthy skin and BCC, obtained from controlled organotypic skin models in the $0.4-1.6$ THz range, are adopted as reference values, since such models provide improved repeatability and reduced biological variability. The corresponding complex permittivity and dielectric contrast are reported in Fig. 17.

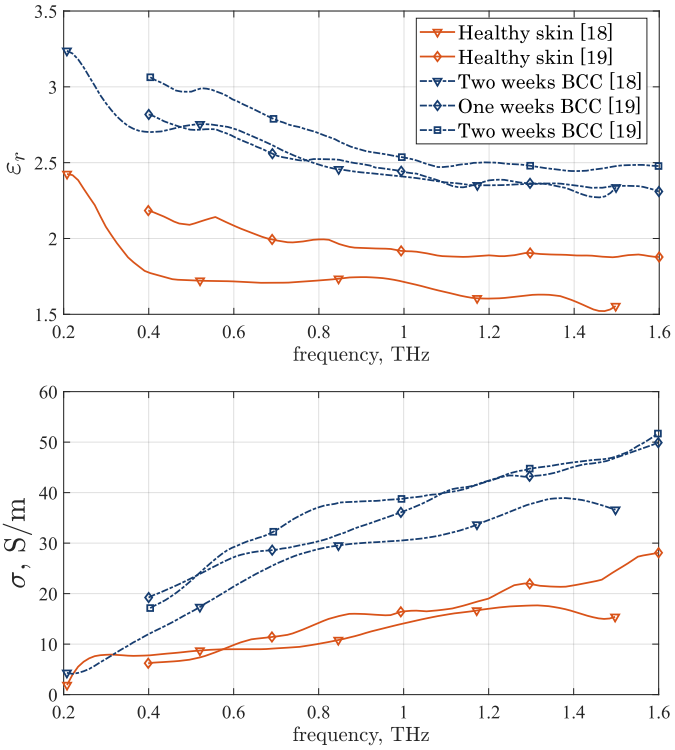


Fig. 17. Dielectric properties of cultured basal cell carcinoma and healthy skin measured via THz-TDS.

Acknowledgment

We would like to acknowledge Dr. Francesco Modica from "Consiglio delle Ricerche - Sistemi e Tecnologie Industriali Intelligenti per il Manifatturiero Avanzato", for the manufacturing of the WR-1.5 waveguide section used to characterize the phantom materials.

References

[1] American Cancer Society. *Cancer Statistics* [Online]. Available: https://cancerstatisticscenter.cancer.org/. Accessed: Nov. 30 2025.

[2] S. Federico, F. Fortarezza, G. Ingravallo, and G. Cazzato, *Skin Cancer - Past, Present and Future*. IntechOpen, 2025, ch. Epidemiology of Skin Cancer in 2024.

[3] Z. Apalla, D. Nashan, R. B. Weller, and X. Castellsagué, "Skin cancer: epidemiology, disease burden, pathophysiology, diagnosis, and therapeutic approaches," *Dermatology and therapy*, vol. 7, no. Issue 1, Supplement, pp. 5–19, 2017.

[4] S. A. R. Naqvi, I. J. Rajmohan, F. Xue, D. Foong, and A. Abbosh, "Electromagnetic Techniques and Systems for Non-Invasive Skin Cancer Detection and Classification: Current Status and Future Perspectives," *IEEE Transactions on Instrumentation and Measurement*, vol. 74, pp. 1–24, 2025.

[5] X. Chen, H. Lindley-Hatcher, R. I. Stantchev, J. Wang, K. Li, A. Hernandez Serrano, Z. D. Taylor, E. Castro-Camus, and E. Pickwell-MacPherson, "Terahertz (THz) biophotonics technology: Instrumentation, techniques, and biomedical applications," *Chemical Physics Reviews*, vol. 3, no. 1, 2022.

[6] H. Elgabarty, T. Kampfrath, D. J. Bonthuis, V. Balos, N. K. Kaliannan, P. Loche, R. R. Netz, M. Wolf, T. D. Kühne, and M. Sajadi, "Energy transfer within the hydrogen bonding network of water following resonant Terahertz excitation," *Science Advances*, vol. 6, no. 17, p. eaay7074, 2020.

[7] A. Mirbeik-Sabzevari, E. Oppelaar, R. Ashinoff, and N. Tavassolian, "High-contrast, low-cost, 3-D visualization of skin cancer using ultra-high-resolution millimeter-wave imaging," *IEEE Transactions on Medical Imaging*, vol. 38, no. 9, pp. 2188–2197, 2019.

[8] A. Christ, A. Aeschbacher, B. Tarigan, N. Chitnis, A. Fallahi, S. Kühn, M. Capstick, and N. Kuster, "Human Skin Model From 15 GHz to 110 GHz," *Bioelectromagnetics*, vol. 46, no. 7, p. e70025, 2025.

[9] F. Töpfer, S. Dudorov, and J. Oberhammer, "Millimeter-wave near-field probe designed for high-resolution skin cancer diagnosis," *IEEE Transactions on Microwave Theory and Techniques*, vol. 63, no. 6, pp. 2050–2059, 2015.

[10] B. Xue, J. Tuomela, K. Haneda, C. Icheln, and J. Ala-Laurinaho, "Permittivity characterization of human skin at sub-THz using free space reflection coefficients," *IEEE Transactions on Microwave Theory and Techniques*, 2024.

[11] K. Y. Chan and R. Ramer, "Novel concept of detecting basal cell carcinoma in skin tissue using a continuous-wave millimeter-wave rectangular glass filled probe," *Medical Devices: Evidence and Research*, pp. 275–285, 2018.

[12] J. J. Young, B. G. Page, A. I. Hernandez-Serrano, J. Hardwicke, and E. Pickwell-MacPherson, "In vivo Terahertz sensing of skin cancer patients," *Advanced Photonics Research*, vol. 6, no. 6, p. 2400195, 2025.

[13] C. S. Joseph, A. N. Yaroslavsky, V. A. Neel, T. M. Goyette, and R. H. Giles, "Continuous wave terahertz transmission imaging of non-melanoma skin cancers," *Lasers in Surgery and Medicine*, vol. 43, no. 6, pp. 457–462, 2011.

[14] X. Qi, K. Bertling, J. Torniainen, F. Kong, T. Gillespie, C. Primiero, M. Stark, P. Dean, D. Indjin, L. Li *et al.*, "Terahertz in vivo imaging of human skin: Toward detection of abnormal skin pathologies," *APL bioengineering*, vol. 8, no. 1, 2024.

[15] V. P. Wallace, A. Fitzgerald, S. Shankar, N. Flanagan, R. Pye, J. Cluff, and D. Arnone, "Terahertz pulsed imaging of basal cell carcinoma ex vivo and in vivo," *British Journal of Dermatology*, vol. 151, no. 2, pp. 424–432, 2004.

[16] R. M. Woodward, B. E. Cole, V. P. Wallace, R. J. Pye, D. D. Arnone, E. H. Linfield, and M. Pepper, "Terahertz pulse imaging in reflection geometry of human skin cancer and skin tissue," *Physics in Medicine & Biology*, vol. 47, no. 21, p. 3853, 2002.

[17] M. Koch, D. M. Mittleman, J. Ornik, and E. Castro-Camus, "Terahertz time-domain spectroscopy," *Nature Reviews Methods Primers*, vol. 3, no. 1, p. 48, 2023.

[18] S. Nourinovin, M. M. Rahman, R. C. Jones, M. P. Philpott, and A. Alomainy, "Impact of drug treatment on the electromagnetic properties of basal cell carcinoma cancer in the Terahertz band," in *2022 16th European Conference on Antennas and Propagation (EuCAP)*. IEEE, 2022, pp. 1–4.

[19] S. Nourinovin, M. M. Rahman, S. J. Park, H. Hamid, M. P. Philpott, and A. Alomainy, "Terahertz dielectric characterization of three-dimensional organotypic treated basal cell carcinoma and corresponding double Debye model," *IEEE Transactions on Terahertz Science and Technology*, vol. 13, no. 3, pp. 246–253, 2023.

[20] J. Lee, C. K. Leung, L. Gingras, R. Holzwarth, D. J. Goodwin, R. M. Dhenge, J. Nassar, P. Bawuah, and J. A. Zeitler, "Improved robustness by concurrent rapid and non-destructive terahertz sensing of pharmaceutical tablet thickness and porosity," *International Journal of Pharmaceutics*, vol. 681, 2025, art. no. 125773.

[21] J. Wang, R. I. Stantchev, Q. Sun, T.-W. Chiu, A. T. Ahuja, and E. P. MacPherson, "Thz in vivo measurements: the effects of pressure on skin reflectivity," *Biomedical optics express*, vol. 9, no. 12, pp. 6467–6476, 2018.

[22] S. Moda, J. A. Tobon Vasquez, G. Virone, and F. Vipiana, "Dielectric Contrast Assessment for Skin Cancer Detection in the Terahertz Band,"

IEEE International Symposium on Antennas and Propagation, Ottawa, Canada, July 2025.
[23] K. Sasaki, E. Porter, E. A. Rashed, L. Farrugia, and G. Schmid, "Measurement and image-based estimation of dielectric properties of biological tissues—past, present, and future—," *Physics in Medicine & Biology*, vol. 67, no. 14, p. 14TR01, 2022.
[24] A. Mirbeik-Sabzevari and N. Tavassolian, "Ultrawideband, stable normal and cancer skin tissue phantoms for millimeter-wave skin cancer imaging," *IEEE Transactions on Biomedical Engineering*, vol. 66, no. 1, pp. 176–186, 2018.
[25] C. Origlia, M. Gugliermino, D. O. Rodriguez-Duarte, J. T. Vasquez, and F. Vipiana, "Anthropomorphic multi-tissue head phantom for microwave imaging devices testing," in *2023 17th European Conference on Antennas and Propagation (EuCAP)*. IEEE, 2023, pp. 1–4.
[26] A. Christ, A. Aeschbacher, F. Rouholahnejad, T. Samaras, B. Tarigan, and N. Kuster, "Reflection properties of the human skin from 40 to 110 GHz: A confirmation study," *Bioelectromagnetics*, vol. 42, no. 7, pp. 562–574, 2021.
[27] Virginia Diodes Inc. "WM-380 (WR1.5) VNAX Mini". Available: https://vadiodes.com/wr1-5vnax-mini/. Accessed: Aug. 27, 2026.
[28] Rhode & Schwarz, "R&S ZNA Vector Network Analyzer Specifications," Available: https://scdn.rohde-schwarz.com/ur/pws/dl_downloads/pdm/cl_brochures_and_datasheets/specifications/5215_4652_22/ZNA_specs_en_5215-4652-22_v2400.pdf, 2026, Accessed: Aug. 27, 2026.
[29] Y. Gao, M. T. Ghasr, M. Nacy, and R. Zoughi, "Towards accurate and wideband in vivo measurement of skin dielectric properties," *IEEE Transactions on Instrumentation and Measurement*, vol. 68, no. 2, pp. 512–524, 2018.
[30] Physik Instrumente (PI) SE & Co. KG, "M-414 Precision High-Load Linear Stage," Available: https://www.pi-usa.us/en/products/precision-motorized-linear-stages/m-414-high-load-precision-stage-701755, Accessed: Aug. 27, 2026.
[31] V. Teppati, A. Ferrero, and M. Sayed, *Modern RF and Microwave Measurement Techniques*. Cambridge University Press, 2013.
[32] Y. Feldman, A. Puzenko, P. Ben Ishai, A. Caduff, I. Davidovich, F. Sakran, and A. J. Agranat, "The electromagnetic response of human skin in the millimetre and submillimetre wave range," *Physics in Medicine & Biology*, vol. 54, no. 11, pp. 3341–3363, 2009.



Stefano Moda (Member, IEEE) received the B.S. and M.S. degrees in biomedical engineering from the Politecnico di Torino, Turin, Italy, in 2020 and 2023, respectively. He is currently pursuing the Ph.D. degree in electrical, electronics, and communications engineering at the Politecnico di Torino. Since 2025, he has been a Research Associate with CNR-IEIIT. In 2026, he was a Visiting Researcher at Technische Universiteit Delft (TU Delft), Delft, The Netherlands, where he conducted research at the THz Sensing Group and the Else Kooi Laboratory. His research interests focus on terahertz (THz) diagnostic imaging techniques for medical applications, including high-frequency dielectric characterization, tissue-mimicking phantom development, and THz measurements. He received the Student Travel Grant at the 2025 IEEE International Symposium on Antennas and Propagation.



Fabio Paonessa (Member, IEEE) was born in Turin, Italy, in September 1985. He received the B.S. and M.S. degrees in biomedical engineering and the Ph.D. degree in electronics engineering from Politecnico di Torino, Turin, Italy, in 2008, 2010, and 2017, respectively.
From 2011 to 2012, he was a Research Assistant at Politecnico di Torino, working on electronic systems for therapeutic ultrasound applications. In 2013, he joined the Institute of Electronics, Information and Telecommunications Engineering (IEIIT) of the Italian National Research Council (CNR), Turin, Italy, where he is currently a Researcher. His research focuses on UAV-based characterization of antenna systems, including low-frequency radio astronomy arrays, Q-band polarimeters, X-band radar systems, and wireless sensor network nodes. His interests also include the design of microwave waveguide passive components and joint communication and sensing at sub-terahertz frequencies. He has authored or coauthored more than 25 journal articles and 50 conference papers and has contributed to several national and international research projects.
Dr. Paonessa was recipient of the Ulrich L. Rohde Innovative Conference Paper Award on Antenna Measurements and Applications, IEEE Antennas and Propagation Society, at the 2018 IEEE Conference on Antenna Measurements and Applications, and the Best Student Paper Award at the 36th European Space Agency Antenna Workshop on Antennas and RF Systems for Space Science.



Jorge A. Tobón Vàsquez (Member, IEEE) received the Degree in electronics engineering from the Universidad de Antioquia, Colombia, in 2010; the master's degree and the Ph.D in electronics and telecommunication from the Politecnico di Torino, Italy, in 2010 and 2014, respectively. Since 2024 he has also worked in Wavision srl (Politecnico di Torino spin-off). His main research activities correspond to modelling, designing, and analyzing systems for microwave imaging applications, and the numerical modelling of complex and nonhomogeneous media propagation. In 2018 received the "Premio Latmiral," an award granted by the Italian Society of Electromagnetism (SIEM). In 2020 he received the URSI General Assembly Scientific Symposium (GASS) Young Scientist Award (YSA) and the Sorrentino URSI Italy National Meeting Young Scientist Paper Award.(Member, IEEE)



Giuseppe Virone (Senior Member, IEEE) was born in Turin, Italy, in 1977. He received the Laurea degree (summa cum laude) in electronic engineering, and the Ph.D. degree in electronics and communication engineering from the Politecnico di Torino, Turin, Italy, in November 2001 and 2006, respectively.
He is currently a Director of Researcher at the Istituto di Elettronica e di Ingegneria Informatica e delle Telecomunicazioni (IEIIT), Italian National Research Council (CNR), Turin. He joined IEIIT as a Research Assistant in 2002. He coordinated more than 25 scientific projects/research units/work-packages funded by both the industry and other scientific research organizations and joined more than 30 research projects as a collaborator. He authored 60 journal papers, 120 conference papers, and three European patents. His activities concern the design, numerical analysis, and characterization of microwave, millimeter passive components and sub-THz components for feed systems, antenna arrays, frequency selective surfaces, compensated dielectric radomes for communication and sensing applications. He is also active in advanced signal processing and propagation measurements for smart radio environments and non-terrestrial networks.



Francesca Vipiana (Senior Member, IEEE) received the Laurea and Ph.D. degrees in electronic engineering from the Politecnico di Torino, Torino, Italy, in 2000 and 2004, respectively, with doctoral research carried out partly at the European Space Research Technology Center, Noordwijk, The Netherlands. From 2005 to 2008, she was a Research Fellow with the Department of Electronics, Politecnico di Torino. From 2009 to 2012, she was the Head of the Antenna and EMC Laboratory, Istituto Superiore Mario Boella, Torino. Since 2012, she has been an Assistant Professor with the Department of Electronics and Telecommunications, Politecnico di Torino, where she has been an Associate Professor since 2014 and a Full Professor since 2021. Her main research activities concern numerical techniques based on integral equations and method of moments, with a focus on multiresolution and hierarchical schemes, domain decomposition, preconditioning and fast solution methods, advanced quadrature integration schemes, and analysis of glide-periodic structures. Moreover, her research interests include the modeling, design, realization and testing of microwave imaging and sensing systems for medical and industrial applications. She received the Lot Shafai Mid-Career Distinguished Award from the IEEE Antennas and Propagation Society (AP-S) in 2017, the Best Paper Award at the Spanish URSI Symposium in 2023, and the Best Electromagnetics Paper Award at the 20th European Conference on Antennas and Propagation (EuCAP) in 2026. She was an Associate Editor of the IEEE Transactions on Antennas and Propagation (2018-2024) and the founder and responsible of the Women in Engineering Column in the IEEE Antennas and Propagation Magazine (2019-2024). She is a member of the EurAAP Board of Directors and the Vice-Chair of the IEEE AP-S Expanding Collaboration & Engagement (ECE) committee.